Influence of Projectile Geometry on Baffled Tube Ram Accelerators

Jason Ginos

A thesis
submitted in partial fulfillment of the
requirements for the degree of

Master of Science in Aeronautics and Astronautics

University of Washington

2023

Committee:

Carl Knowlen, Chair

Dana Dabiri

Program Authorized to Offer Degree:
Aeronautics and Astronautics

University of Washington

Abstract

Influence of Projectile Geometry on Baffled Tube Ram Accelerators

Jason Ginos

Chair of the Supervisory Committee:
Carl Knowlen

The ram accelerator is a hypervelocity mass driver that operates on a principle similar to that of a ramjet in tube. It is capable of accelerating projectiles to velocities in excess of 2.6 km/s and has applications in direct space launch, impact assisted drilling, and defense. The baffled tube ram accelerator is a derivative of the ram accelerator that was invented in order to enlarge the operational envelope by enabling a lower start velocity and allowing for the use of propellant mixtures with higher heat release. The influence of projectile geometry on baffled tube ram accelerators was experimentally investigated in an effort to identify the optimum projectile geometry. Geometric variations included the nosecone angle, tailcone angle, projectile shoulder diameter, and projectile shoulder length. Performance was evaluated based on total delta-v, thrust produced, and projectile stability. Results indicate that nosecone performance has a Mach number dependence. Short nose projectiles produced higher relative thrust at low Mach numbers while long nose projectiles had higher relative thrust at high Mach numbers. Thrust was found to increase with increasing tailcone length. Thrust is maximized at approximately 92% projectile shoulder-to-baffle bore ratio, and was shown to increase with increasing shoulder length.

TABLE OF CONTENTS

LIST OF FIGURES

LIST OF TABLES

GLOSSARY

Acronyms and Subscripts

1: Entrance plane

2: Exit plane

b: Tube bore

TCRA: Thermally Choked Ram Accelerator

SBRA: Smooth Bore Ram Accelerator

BTRA: Baffled Tube Ram Accelerator

Variables

F : Thrust, N

p : Pressure, Pa

A : Area, m^2

ρ : Density, kg/m^3

u : Velocity, m/s

M : Mach number

a : Sound speed, m/s

R : Gas constant, $\frac{kJ}{kg \cdot K}$

T : Temperature, K

γ : Ratio of specific heats

Δq : Heat release, kJ/kg

Δh_f^0 : Enthalpy of formation, kJ/kg

h : Specific enthalpy, kJ/kg

c_p : Specific heat at constant pressure, $\frac{kJ}{kg \cdot K}$

Q : Non-dimensional heat release

I : Non-dimensional thrust

D : Drag, N

η_c : Combustion efficiency

ACKNOWLEDGMENTS

First and foremost, I want to thank Dr. Carl Knowlen for offering me this tremendous opportunity to work in the UW Ram Accelerator Lab over the last two years. Through his mentorship, I have learned about compressible fluids, propulsion, gas dynamics, and more ram history than I can comfortably recite. I was constantly impressed by his passion for the project and his joy and patience in sharing that passion with others.

Next, I want to thank all my fellow grad and undergrad students in the lab. Brian, John, Desiree, Cullen, Richard, Shahrez, Carter, Misae, Tommy, Victor, Raiden, Ben (all three of you), Ali, Kevin, James, Casey, Connor, and Justin. I am especially grateful to Brian, John, Desiree, and Richard who all taught me how to run the ram accelerator. Having the opportunity to learn and work alongside you all has been an absolute blast.

Lastly, I want to thank Dr. Dana Dabiri for serving on my committee and sharing his insights on my work and Pipeline2Space for their support of the UW Ram Accelerator lab.

Ramo Ergo Sum

DEDICATION

To all those who believed in me when I did not believe in myself

Chapter 1

INTRODUCTION

The ram accelerator is a hypervelocity mass driver capable of accelerating projectiles to velocities in excess of 2.6 km/s [1]. Research at the University of Washington (UW) began in the mid-1980s with the construction of a 16 meter long test section having a 38-mm bore [2]. Unlike a traditional gun, where the projectile is propelled by expanding gas that continuously decreases in pressure as shown in Figure 1.1, the ram accelerator is propelled by a pressure wave that moves with the projectile and thereby provides a continuous acceleration.

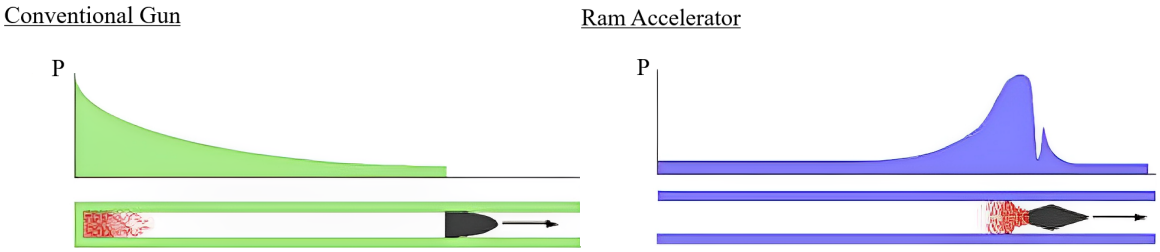

Figure 1.1: Comparison of gun and ram pressure waves

This has significant benefits for scalability, since a higher exit velocity can be obtained by simply lengthening the system. Due to its hypervelocity capability and scalability, the ram accelerator has potential for use in a number of applications including direct space-launch, defense, and impact assisted drilling [3, 4].

1.1 Principles of Operation

The ram accelerator operates on a principle similar to that of a ramjet or scramjet Fig. 1.2, wherein a cylindrical projectile with a conic nosecone is accelerated to supersonic velocity prior to entering a pressurized mixture of combustible gases Fig. 1.3. In this manner the

projectile nose acts like the centerbody on a ramjet with the tube wall in place of the outer cowling.

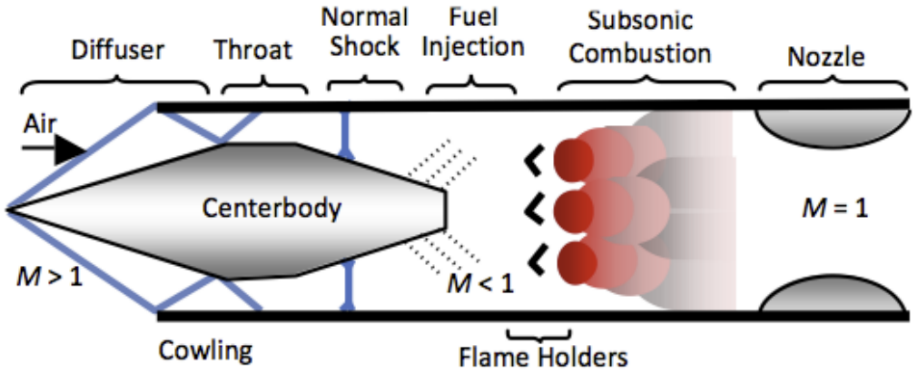

Figure 1.2: Conventional ramjet propulsive cycle

Ram accelerators can operate in several different velocity regimes including sub-detonative, trans-detonative, and super-detonative [5]. These modes differ with regard to the projectile velocity relative to the Chapman-Jouguet (CJ) detonation velocity. The focus of this investigation is on the Thermally Choked Ram Accelerator (TCRA), which operates in the sub-detonative velocity regime.

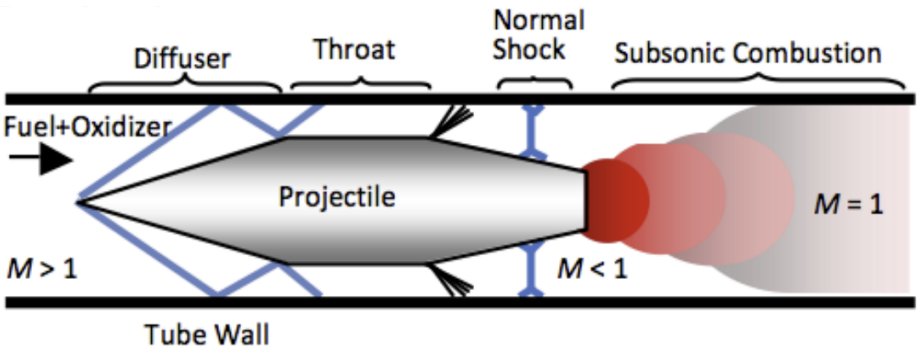

Figure 1.3: Thermally choked ram accelerator propulsive cycle

1.2 Thermally Choked Ram Accelerator

Operation of the thermally choked ram accelerator begins by launching the projectile such that the Mach number at the projectile throat is greater than one with respect to the in-tube propellant. Once through the throat, a system of shocks decelerates the supersonic flow and initiates subsonic combustion on the flat base of the projectile. The energy release increases the temperature while accelerating the flow to a thermally choked state. This end state condition acts like a flow constricting nozzle in an air-breathing ramjet to maintain the high-pressure shock system on the aftbody of the projectile. Stable operation in this state is bounded by three limits, a minimum Mach number, a maximum heat release, and a minimum heat release limit as shown in Figure 1.4 [6].

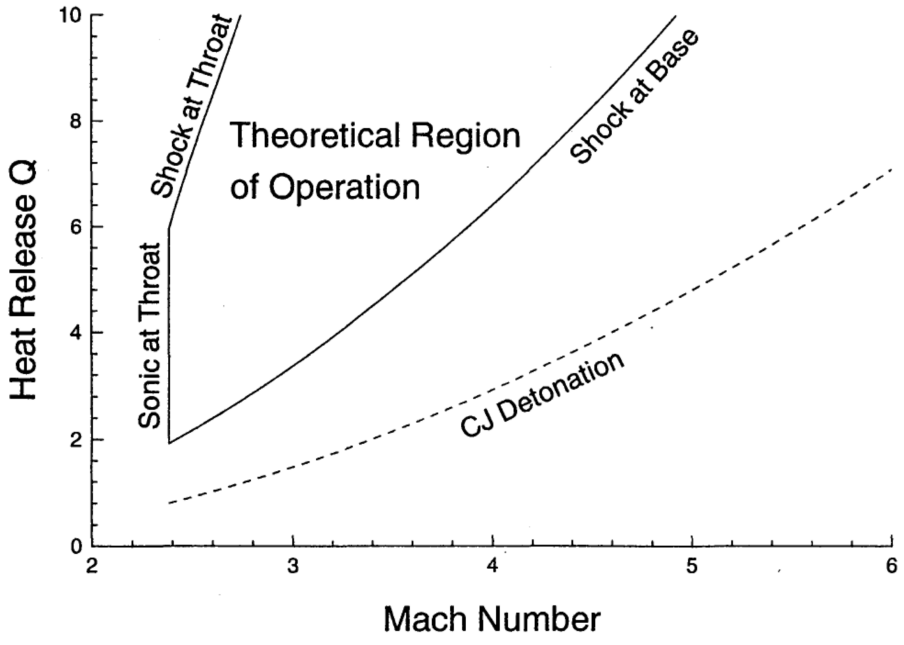

Figure 1.4: TCRA performance envelope.

Below the minimum Mach number limit, the flow will choke at the projectile throat, imposing subsonic flow over the nosecone of the projectile. The maximum heat release limit is dependent on the projectile's ability to contain the combustion wave and prevent it from

passing through the throat. This event, which is known as an "unstart", is controlled by propellant heat release, pressure, and other geometric factors. The final limit, minimum heat release, is defined by the heat release necessary to drive the shock system at pace with the projectile. Dropping below this limit results in wave fall-off and a cessation of thrust.

1.3 Baffled Tube Ram Accelerator

The baffled tube ram accelerator was invented in 2005 in order to enlarge the operating range of the ram accelerator [7]. Research has since shown that it is successful in increasing the maximum propellant heat release and decreasing the required start velocity [1]. This is achieved by having each baffle separated by a constriction that serves to push back or "sweep" the shock off the tail of the projectile, thereby preventing an unstart.

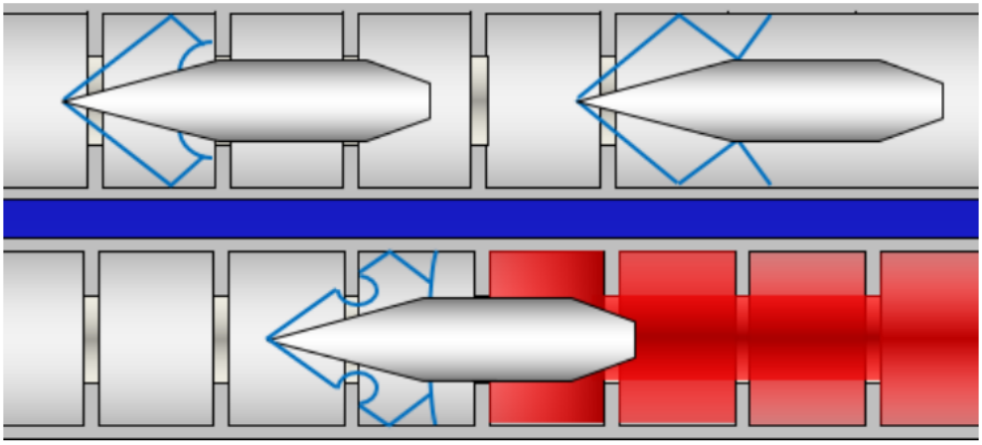

Figure 1.5: Evolution of the BTRA flowfield.

The BTRA also offers the advantage of using axisymmetric projectiles since the fins traditionally machined into the projectile for stability can instead be incorporated into the baffle structure as rails. This allows for projectiles which are much simpler and cheaper to manufacture.

1.4 Prior Investigations

Prior work has researched the impacts of projectile geometry on Smooth Bore Ram Accelerator (SBRA) performance. This included nose and tail angle variations, diameter variation, length variation, and fin number variation [8]. In the BTRA system, some work has been done to investigate the impact of projectile shoulder length [9], and diameter [10], however there has been no comprehensive geometry investigation as was done with the SBRA. The intent of this thesis is to expand on the prior shoulder length series by investigating variations in projectile nose angle, tail angle, and diameter. In this manner, we hope to identify the "ideal" projectile geometry for BTRA operation.

Chapter 2

THEORY

This chapter will present and discuss the theory used to model and predict ram accelerator performance. We begin by discussing the characteristics of the Thermally Choked Ram Accelerator before presenting the basic Smooth Bore Ram Accelerator model and then extending to the Baffled Tube Ram Accelerator case. This will give us a foundation for discussing ram performance and how theory accounts for variations in projectile geometry.

2.1 Thermally Choked Ram Accelerator

The TCRA propulsive cycle has a heat addition that occurs subsonically and is bounded by a thermally choked plane. When modeled in the projectile frame of reference as shown in Figure 2.1, premixed fuel and oxidizer enter the control volume at plane 1 where they are compressed by a series of shocks while flowing over the projectile. This results in combustion occurring in the subsonic region behind the projectile that can be modeled as constant area heat addition. The combustion causes an increase in pressure at the base of the projectile while also increasing propellant velocity resulting in a thermally choked sonic state at the exit plane (2).

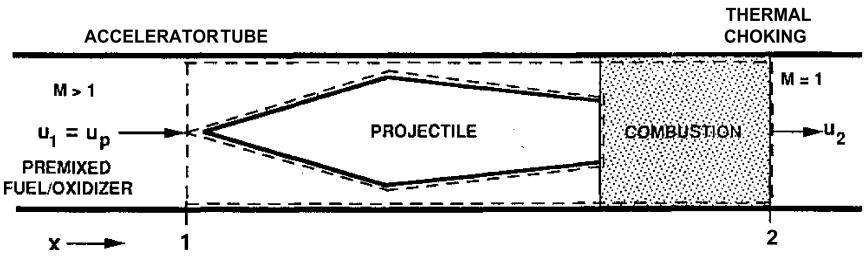

Figure 2.1: Thermally choked ram accelerator control volume

Prior analysis has shown that, for accelerations of less than 20,000 g, the effects of

projectile acceleration are negligible and the TCRA can be modeled using a quasi-steady flow assumption [11].

2.1.1 Smooth Bore Ram Accelerator

Ram accelerator research began with the SBRA that utilizes a smooth bore tube much like a traditional gun. This smooth wall configuration allows us to neglect drag force on the projectile, thereby simplifying the theory [12]. We will present here the black box model used to calculate non-dimensional thrust in the SBRA.

To begin, we assume 1D quasi-steady flow and apply conservation of momentum to the TCRA control volume shown in Figure 2.1. This allows us to describe the thrust, F on the projectile as follows:

$$F = \left(p_2 A_2 + \rho_2 u_2^2 A_2\right) - \left(p_1 A_1 + \rho_1 u_1^2 A_1\right) \tag{2.1}$$

Since the SBRA has no changes in area, we can normalize this expression by fill pressure, p_1 and bore area, A_b, to yield:

$$\frac{F}{p_1 A_b} = \left(\frac{p_2}{p_1} + \frac{\rho_2}{p_1} u_2^2\right) - \left(1 + \frac{\rho_1}{p_1} u_1^2\right) \tag{2.2}$$

We express flow velocity, u, in terms of local Mach number and sound speed, a, as $u = Ma$:

$$\frac{F}{p_1 A_b} = \left(\frac{p_2}{p_1} + \frac{\rho_2}{p_1} M_2^2 a_2^2\right) - \left(1 + \frac{\rho_1}{p_1} M_1^2 a_1^2\right) \tag{2.3}$$

If we assume all propellants act as ideal gases, then $p = \rho RT$. Since the sound speed can be expressed as, $a = \sqrt{\gamma RT}$, we see that:

$$\frac{F}{p_1 A_b} = \frac{p_2}{p_1}\left(1 + \gamma_2 M_2^2\right) - \left(1 + \gamma_1 M_1^2\right) \tag{2.4}$$

We can express the pressure ratio using the ideal gas law:

$$\frac{p_2}{p_1} = \frac{\rho_1 R_1 T_1}{\rho_2 R_2 T_2} \tag{2.5}$$

From conservation of mass, we know that:

$$\rho_1 u_1 = \rho_2 u_2 \tag{2.6}$$

Substituting into Eq. 2.5 yields:

$$\frac{p_2}{p_1} = \frac{u_2 R_1 T_1}{u_1 R_2 T_2} \tag{2.7}$$

Since $a = \sqrt{\gamma RT}$, we can rewrite the above expression as follows:

$$\frac{p_2}{p_1} = \frac{M_1 \sqrt{\gamma_1 R_2 T_2}}{M_2 \sqrt{\gamma_2 R_1 T_1}} \tag{2.8}$$

Next, we apply conservation of energy:

$$\rho_1 u_1 A_1 \left(h_1 + \frac{u_1^2}{2} + \Delta q \right) = \rho_2 u_2 A_2 \left(h_2 + \frac{u_2^2}{2} \right) \tag{2.9}$$

where $\Delta q = \Delta h_f^0$, the change in enthalpy of formation at $T_{ref} = 0$ K. From conservation of mass, $\rho_1 u_1 A_1 = \rho_2 u_2 A_2$, and thus:

$$h_1 + \frac{u_1^2}{2} + \Delta q = h_2 + \frac{u_2^2}{2} \tag{2.10}$$

This can be rewritten in terms of Mach number as:

$$h_1 + \frac{M_1^2 \gamma_1 R_1 T_1}{2} + \Delta q = h_2 + \frac{M_2^2 \gamma_2 R_2 T_2}{2} \tag{2.11}$$

Next, we nondimensionalize the expression by dividing through $c_{p1} T_1$. This introduces a new variable, $Q = \frac{\Delta q}{c_{p1} T_1}$, to describe nondimensional heat release:

$$\frac{h_1}{c_{p1} T_1} + \frac{M_1^2 \gamma_1 R_1}{2 c_{p1}} + Q = \frac{h_2}{c_{p1} T_1} + \frac{M_2^2 \gamma_2 R_2 T_2}{2 c_{p1} T_1} \tag{2.12}$$

Mayer's relation states that $c_v = c_p - R$ and thus, $c_p = \frac{\gamma R}{\gamma - 1}$. This allows us to simplify as follows:

$$\frac{h_1}{c_{p1} T_1} + \frac{\gamma_1 - 1}{2} M_1^2 + Q = \frac{h_2}{c_{p1} T_1} + \frac{\gamma_2 - 1}{2} M_2^2 \frac{c_{p2} T_2}{c_{p1} T_1} \tag{2.13}$$

This can be solved for the temperature ratio to yield:

$$\frac{T_2}{T_1} = \frac{c_{p1}}{c_{p2}} \left(\frac{\frac{h_1}{c_{p1} T_1} + M_1^2 \frac{\gamma_1 - 1}{2} + Q}{\frac{h_2}{c_{p2} T_2} + M_2^2 \frac{\gamma_2 - 1}{2}} \right) \tag{2.14}$$

We then combine Eq. 2.14 with Eq. 2.8 and plug the resulting expression into Eq. 2.4 to find:

$$\frac{F}{p_1 A_b} = \left(1 + \gamma_2 M_2^2 \right) \frac{M_1}{M_2} \frac{\gamma_1}{\gamma_2} \sqrt{\left(\frac{\gamma_2 - 1}{\gamma_1 - 1} \right) \left(\frac{\frac{h_1}{c_{p1} T_1} + M_1^2 \frac{\gamma_1 - 1}{2} + Q}{\frac{h_2}{c_{p2} T_2} + M_2^2 \frac{\gamma_2 - 1}{2}} \right)} - \left(1 + \gamma_1 M_1^2 \right) \tag{2.15}$$

Lastly, since the TCRA defines the exit plane to be thermally choked with $M_2 = 1$ the non-dimensional smooth bore thrust, I_{SBRA}, is:

$$I_{SBRA} = \frac{F}{p_1 A_b} = M_1 (1+\gamma_2) \frac{\gamma_1}{\gamma_2} \sqrt{\left(\frac{\gamma_2 - 1}{\gamma_1 - 1}\right) \left(\frac{\frac{h_1}{c_{p1}T_1} + M_1^2 \frac{\gamma_1 - 1}{2} + Q}{\frac{h_2}{c_{p2}T_2} + \frac{\gamma_2 - 1}{2}}\right)} - \left(1 + \gamma_1 M_1^2\right) \tag{2.16}$$

Equation 2.16 describes projectile thrust as a function of inlet Mach number, M_1, nondimensional heat release, Q, and the thermodynamic parameters, γ, and $\frac{h}{c_p T}$ at the entrance and exit planes of the control volume. Note, the SBRA model for TCRA thrust does not include any projectile geometry specifications, and that its predictions are independent of projectile shape. This model has been shown to agree well with experiments in the Mach number range of 2.5 to 4 while using many different propellants at several different bore sizes [11, 13, 14, 15].

2.1.2 The Baffled Tube Ram Accelerator

The Baffled Tube Ram Accelerator is an evolution of the SBRA configured to allow higher heat release propellants, lower start velocities and enable the use of axisymmetric projectiles. Prior work has shown that, unlike the SBRA, the BTRA thrust is best modeled with an added drag term, D, as well as a correction for combustion effectiveness, $Q_{eff} = \eta_c Q$ [16].

$$I_{BTRA} = \frac{F + D}{p_1 A_b} = M_1 (1+\gamma_2) \frac{\gamma_1}{\gamma_2} \sqrt{\left(\frac{\gamma_2 - 1}{\gamma_1 - 1}\right) \left(\frac{\frac{h_1}{c_{p1}T_1} + M_1^2 \frac{\gamma_1 - 1}{2} + \eta_c Q + \frac{D(\gamma - 1)}{p_1 A_b \gamma_1}}{\frac{h_2}{c_{p2}T_2} + \frac{\gamma_2 - 1}{2}}\right)} - \left(1 + \gamma_1 M_1^2\right) \tag{2.17}$$

The drag term in Eq. 2.17 is designed to account for both projectile-flowfield interactions as well as interactions between the flowfield and baffles themselves, while the combustion effectiveness is meant to account for the fact that useful heat release imparted to the projectile is less than theoretical propellant heat release due to baffle interactions. Prior analysis for both of these terms was conducted through empirical curve-fitting [16].

2.2 Geometric Considerations

Now that we have a basic understanding of the theory used to model BTRA operation, we can use this to predict how changes in projectile geometry may impact performance. There are four main geometric parameters to be considered, nosecone angle, tailcone angle, projectile diameter, and projectile shoulder length. Varying these parameters should have impacts on projectile acceleration due to changes in thrust, drag, and mass. Additionally, variations in these parameters can impact the stable operational envelope of the ram accelerator which is largely determined by the projectiles ability to contain the combustion wave and prevent an unstart from occurring.

2.2.1 Nosecone

In examining Eq. 2.17, we see that BTRA performance could be optimized based on the drag term, D. Based on this theory, we expect that drag on the projectile would decrease with increasing nosecone angle. This will however also necessitate an increase in projectile mass. One other consideration is structural integrity of projectile. There is reason to suspect that excessive heat transfer at high Mach numbers leads to blunting or folding of the nosecone which has negative impacts on performance and can lead to catastrophic failure. Longer nosecones will be more susceptible to this degradation which when combined with the resulting mass penalty, may impose an upper limit on useful nose angle.

2.2.2 Tailcone

Since drag is not a major factor on the tail of the projectile, theory suggests that projectiles could be optimized by decreasing tailcone angle in order to decrease overall projectile mass. However, a change in tailcone may also have impacts on projectile stability, in particular, the projectiles ability to contain the combustion wave and prevent an unstart.

2.2.3 Diameter

In addition to having an impact on overall mass, projectile diameter is thought to play a larger role in stabilizing operation. When considering the stable operational envelope, the

parameter of interest is the the area ratio A_{throat}/A_{bore}. Increasing the projectile diameter decreases the throat area which should allow for a higher heat release at a given Mach number since the combustion will be more contained. This will however have a negative impact on the minimum Mach number necessary for starting operation. Conversely, decreasing the projectile diameter increases the throat area which will limit the usable heat release while decreasing the minimum start Mach.

2.2.4 Shoulder Length

Prior work has shown that increasing projectile shoulder length leads to an increase in thrust [9]. This is thought to be due to the fact that a longer shoulder length allows for a longer residence time for the combusting propellant that thereby increases the overall thrust delivered at a given heat release. Alternatively, the increase could be due to the added canting stability that longer projectiles benefit from, which could decrease flowfield drag and friction due to rail interactions.

Chapter 3

EXPERIMENT

This chapter disscusses the experimental facility used to conduct all three test series, as well as the methods and procedures used in experiment setup. Also detailed are the geometry variations themselves.

3.1 Experimental Facility

All tests were conducted at the UW ram accelerator facility. The facility consists of a light gas gun, launch tube, eight 2-m-long instrumented test sections (38-mm-bore), and a catcher tube as shown in Figure 3.1.

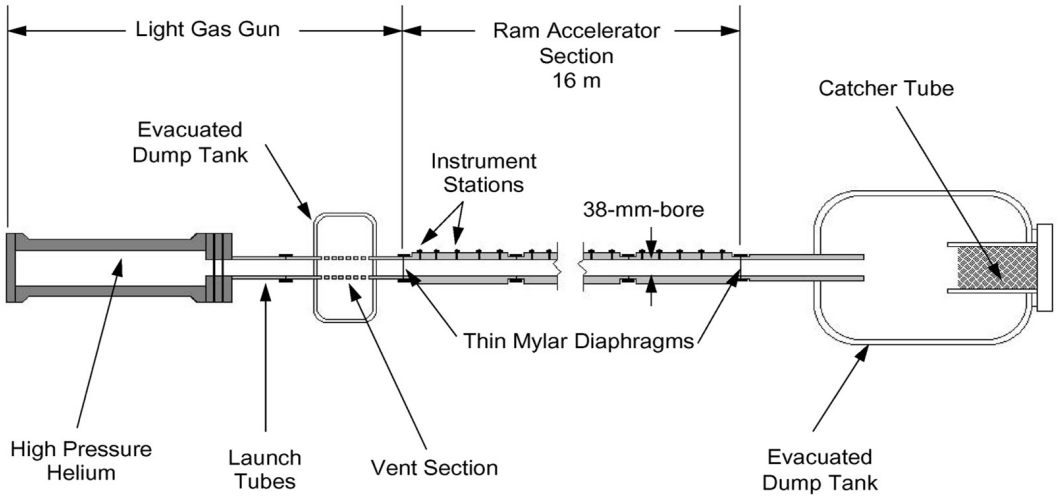

Figure 3.1: UW ram accelerator facility

The ram accelerator experiment begins with the light gas gun used to launch the test

projectile from rest to its supersonic entrance velocity. The required entrance velocity for succesfully starting the BTRA propulsive cycle can vary based on propellant sound speed and baffle configuration. Following its launch from the light gas gun, the projectile transits an evacuated launch tube and passes through a vent tank to strip the helium propelling it. It then punctures a Mylar diaphragm to enter the first ram stage where it initiates combustion and begins accelerating. The projectile continues to accelerate as it traverses the ram stages until it exits by puncturing a final Mylar diaphragm and entering an evacuated drift tube (which allows for accurate exit velocity measurements). After coasting through the drift tube, the projectile enters a final dump tank and is brought to rest by a catcher tube filled with rolled carpet and steel plates.

3.1.1 Instrumentation

Experimental data is logged at 1.25 MHz by a National Instruments PXIe-1071 chassis with two PXIe-6358 modules. The ram stages are all instrumented with piezoelectric pressure transducers (PCB119) used to read the projectile pressure history and custom-built electromagnetic probes that are used to detect the presence of a neodymium magnet installed within the projectile. The mag-probe passage time can be combined with accurate distance measurements between stations that allows for the velocity-distance history of the projectile to be plotted.

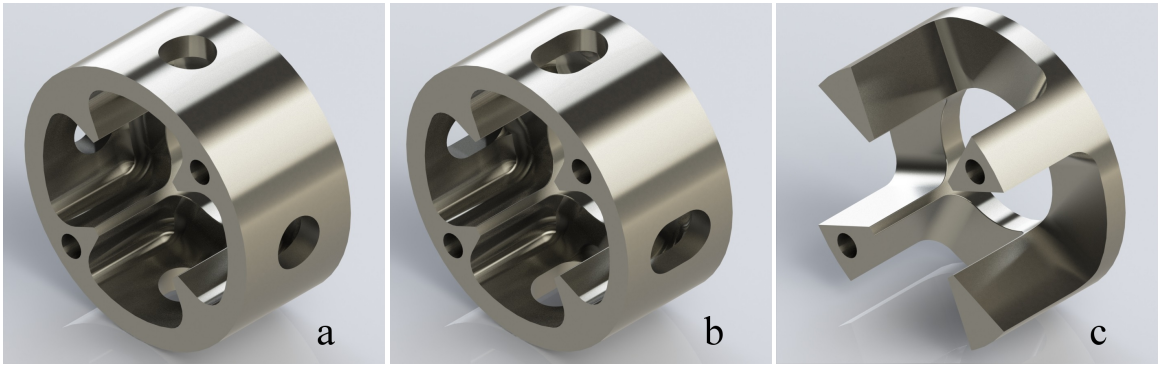

Figure 3.2: The 501 (a), 501s (b), and 111 (c) baffle designs.

3.1.2 Baffle Configuration

The 8-m-long ram test section was filled with three different baffle designs. These are the BTRA 501, BTRA 501s, and BTRA 111 baffle inserts shown in Figure 3.2. Each 2-m-long BTRA tube contains 56 baffle inserts with the same length (1.406-in) and bore diameter (1.502-in) but varying in shape and volume. The nosecone, tailcone, and diameter series were all conducted with the baffle configuration shown in Figure 3.3. The prior shoulder length series was conducted in a different configuration wherein some of the 501s baffles were swapped with 501 baffles [9].

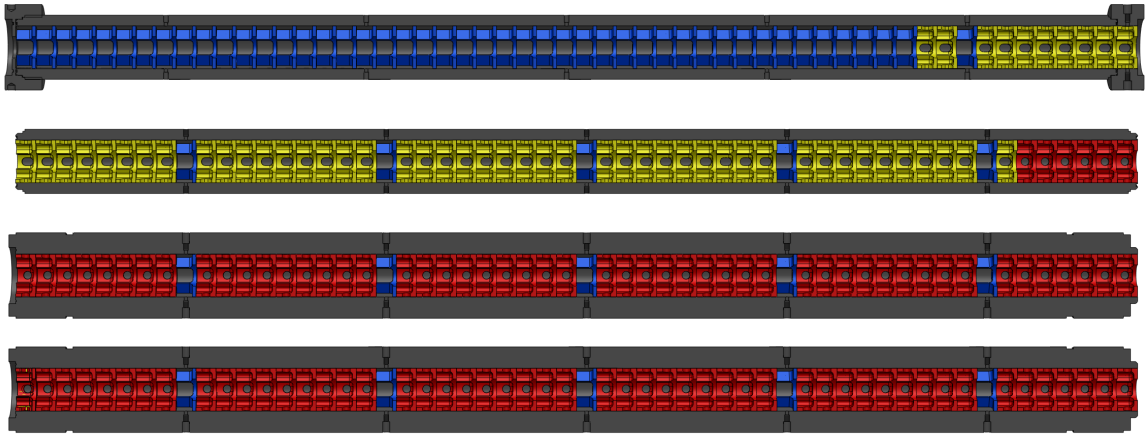

Figure 3.3: Baffle Configuration, Blue = 111, Yellow = 501s, Red = 501

3.2 Experimental Method

3.2.1 Fueling Procedure

Each ram shot began with the sealing of the system such that the four BTRA tubes were joined into one constant 8-m-long section bounded on either end by diaphragms that separated the upstream launch tube and downstream drift tube. Prior to propellant loading, all three sections (launch tube, ram stages, and drift tube) were evacuated to less than 1 Torr. All three geometry variation series were fired into the same propellant mixture:

$$CH_4 + 2O_2 + 4.67N_2$$

Fueling was controlled by three mass flow controllers (fuel, diluent, and oxidizer). Propellant loading began by allowing all three mass flow controllers to flow out a dump line until proper flow rate was established. All fill pressures were 300 psig for these experiments.

3.2.2 Firing Procedure

Initial launch velocity was provided by a helium light gas gun. Target inlet velocity was nominally 900 m/s (nosecone and tailcone series) or 850 m/s (diameter series). Launch velocity was controlled by varying the breech pressure in the light gas gun. Gun pressures were determined by linearly scaling from prior shots. Exact break pressure was controlled by using scribed aluminum diaphragms in a double-diaphragm configuration where the breech was filled to target launch pressure and the interdiaphragm was filled to an intermediate value as shown in Figure 3.4.

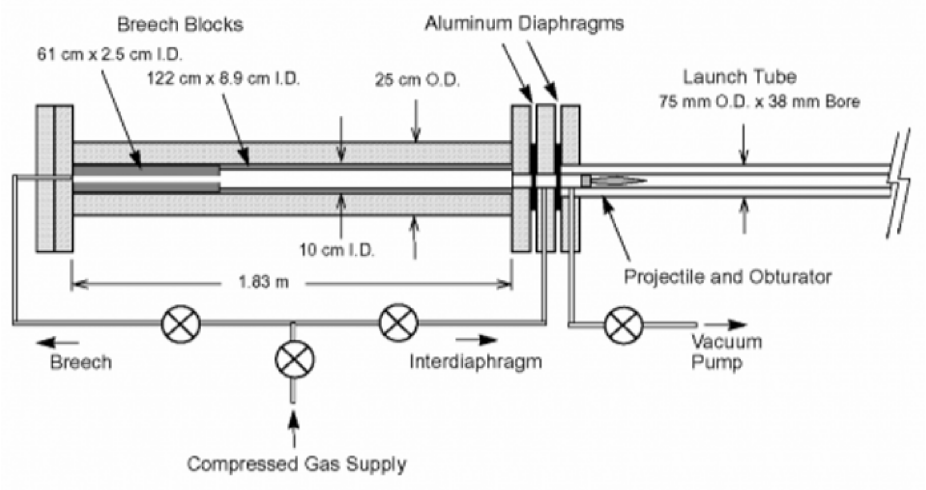

Figure 3.4: Light gas gun with double diaphragm launch control

Initial pressurization of the breech and interdiaphragm sections occurred concurrently until the desired interdiaphragm pressure had been reached at which point it would be isolated and pressurization would continue in the breech. Launch pressures in excess of 4000 psi required a pump to fully pressurize the breech. Since variations in the pump dynamic pressure would induce uncertainties in actual firing pressure, the breech section

was over-pressurized by approximately 50 psi, then the pump was shut off and the shot was fired by venting the interdiaphragm volume to atmosphere when the breech pressure had dropped to its target value.

3.3 Projectile Configurations

The projectile geometry variations consist of three different series. The nosecone angle series, where nose angle was varied from 9°-18°. The tailcone angle series, where tail angle was varied from 9°-18°. And the diameter series, where the diameter was varied from 1.34-1.42 inches.

3.3.1 Nosecone Angle Series

All projectiles in the nosecone variation series had a standard diameter of 1.38 inches (which prior work had found to be optimal) [10], shoulder length of 2.812 inches (2BL), and a constant tail angle of 12°. A summary of the projectile specifications can be seen in Table 3.1.

Table 3.1: Nosecone Series

Projectile	Diameter (in)	Tail Angle (°)	Nose Angle (°)	Mass (g)
P380-2BL-12-09	1.38	12	9	156
P380-2BL-12-12	1.38	12	12	144
P380-2BL-12-15	1.38	12	15	137
P380-2BL-12-18	1.38	12	18	132

3.3.2 Tailcone Angle Series

All projectiles in the tailcone variation series had a standard diameter of 1.38 inches, shoulder length of 2.812 inches (2BL), and a constant nose angle of 15°. A summary of the projectile specifications can be seen in Table 3.2.

Table 3.2: Tailcone Series

Projectile	Diameter (in)	Tail Angle (°)	Nose Angle (°)	Mass (g)
P380-2BL-09-15	1.38	9	15	145
P380-2BL-12-15	1.38	12	15	137
P380-2BL-15-15	1.38	15	15	131
P380-2BL-18-15	1.38	18	15	127

3.3.3 Diameter Series

All projectiles in the diameter variation series had a standard tail angle of 12° and nose angle of 15°. The shoulder length for each projectile was chosen to prevent the cant angle from exceeding a maximum value of 1.66°. A summary of the projectile specifications for this test series can be seen in Table 3.3.

Table 3.3: Diameter Series

Projectile	Diameter (in)	Shoulder Length (in)	Mass (g)
P340-3BL-12-15	1.34	4.218	166
P360-3BL-12-15	1.36	4.218	170
P380-3BL-12-15	1.38	4.218	178
P400-2.5BL-12-15	1.40	3.515	163
P420-2.5BL-12-15	1.42	3.515	169

P380-2BL-12-18

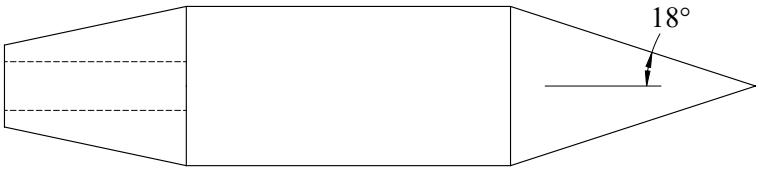

P380-2BL-12-15

P380-2BL-12-12

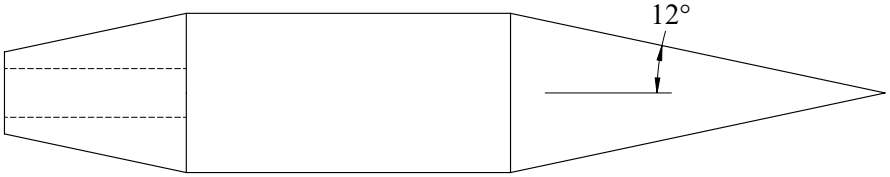

P380-2BL-12-09

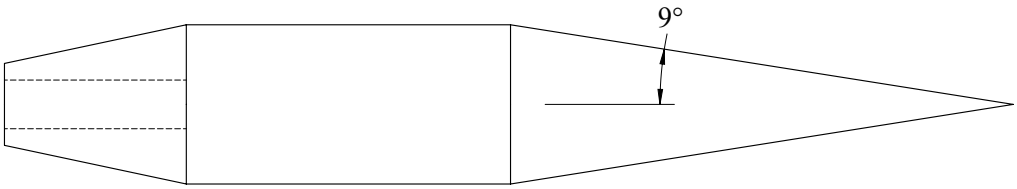

Figure 3.5: Nosecone Angle Variations

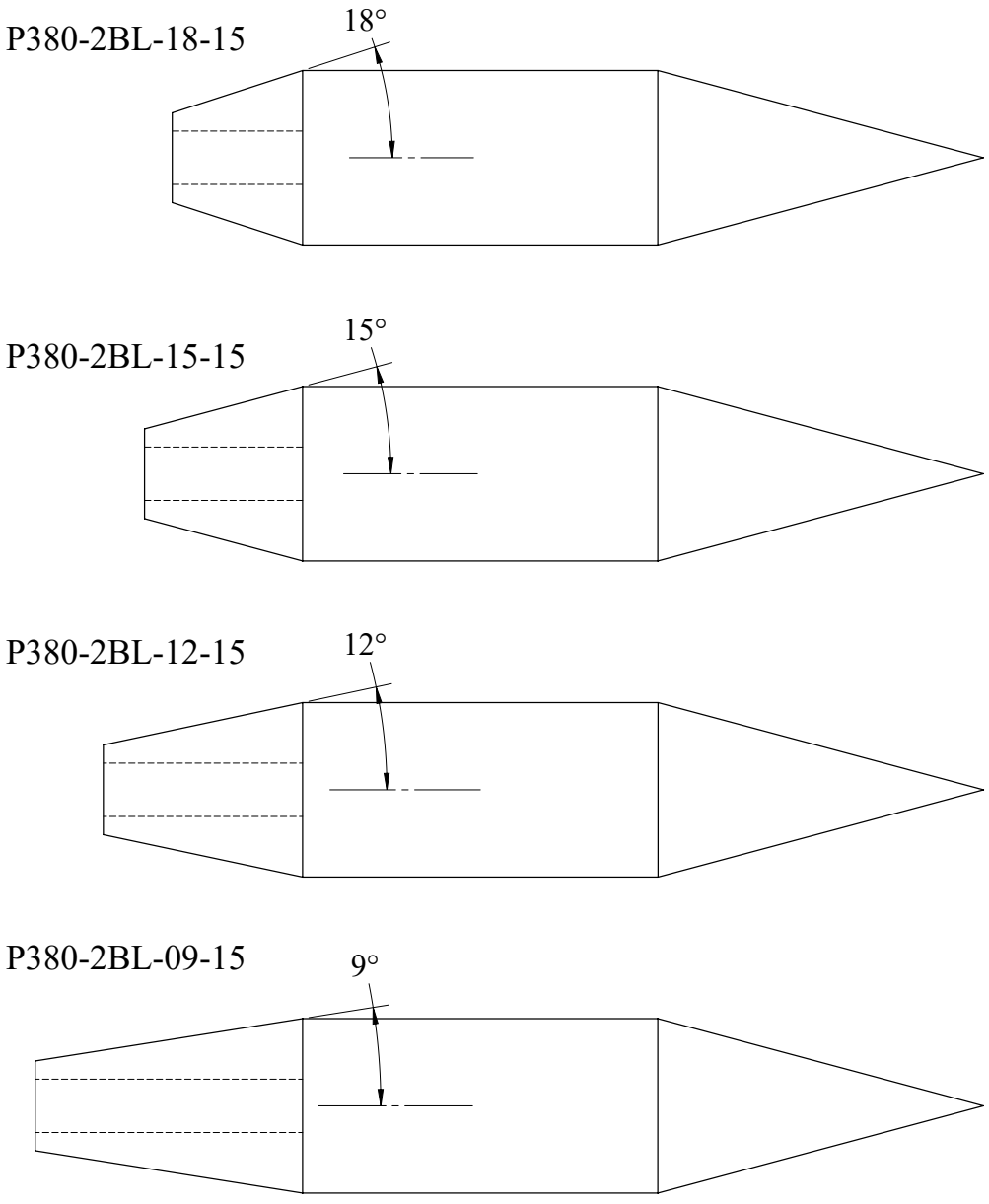

Figure 3.6: Tailcone Angle Variations

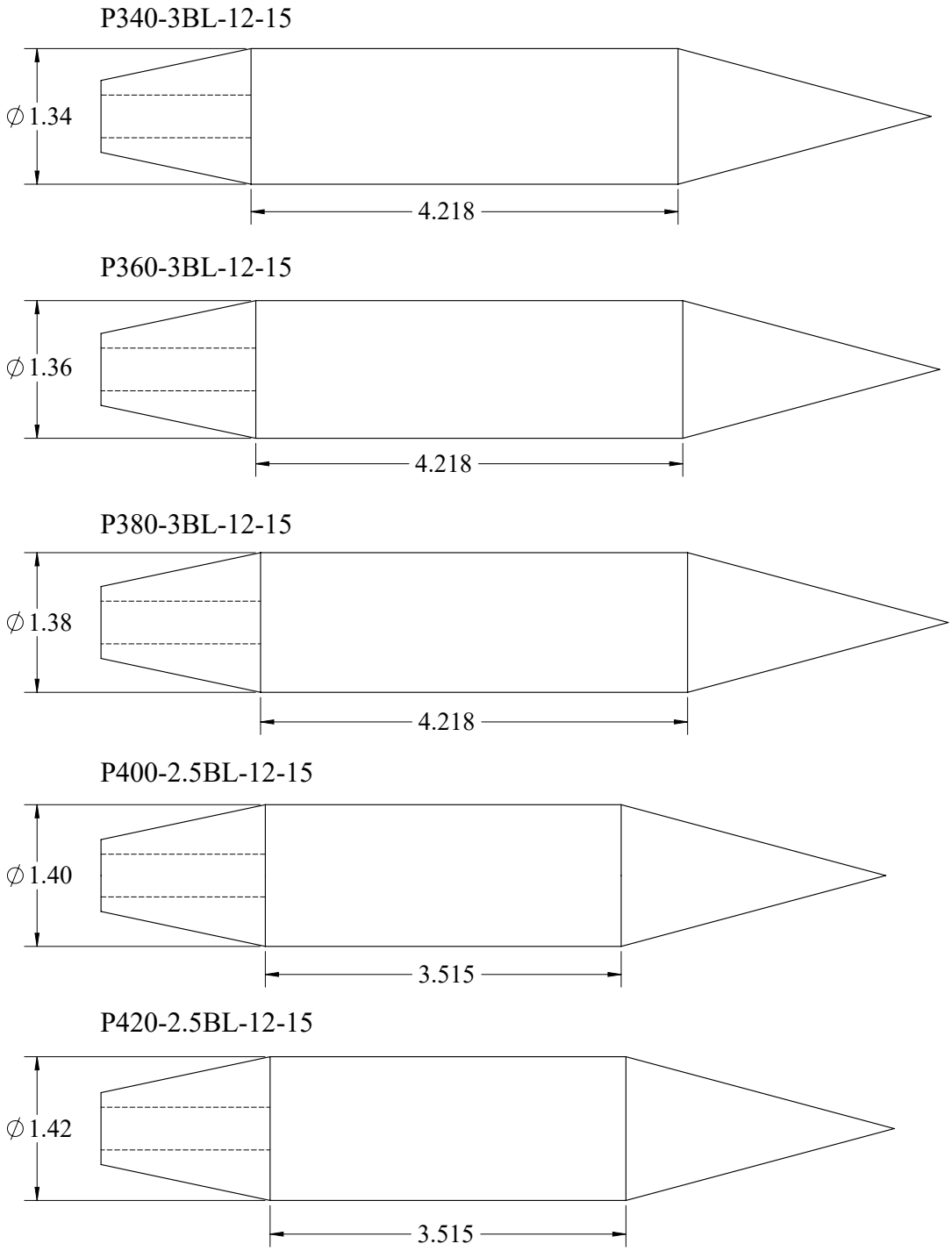

Figure 3.7: Diameter Variations

Chapter 4

DATA AND ANALYSIS

In this chapter we will present and analyze the data collected in the nosecone, tailcone, and diameter geometry series and compare with prior diameter and shoulder length data.

4.1 Experimental Data

4.1.1 Nosecone Series

The nosecone series consisted of data from six individual shots that included all four variations and two repeated shots. Velocity distance data are plotted in Figure 4.1.

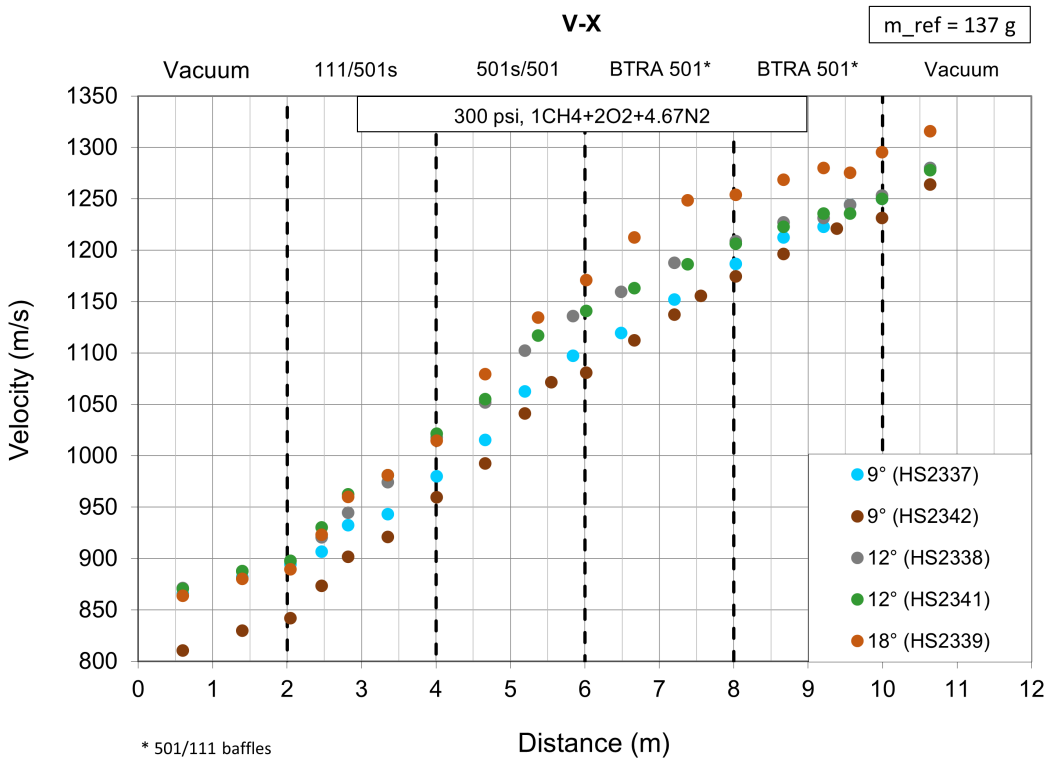

Figure 4.1: Nosecone velocity-distance data

The entrance velocities ranged from 842 to 898 m/s in this series of experiments. The highest exit velocity was $V_{out} = 1295$ m/s and was observed with the 18° nosecone (P380-2BL-12-18) which also had the greatest total delta-v at 406 m/s. A plot of thrust vs. Mach (averaged over each of the 2-m stages) is shown in Figure 4.2. Note that the 15° nosecone reference projectile was excluded from these plots due to variance in its performance that implied severe projectile degradation had occurred.

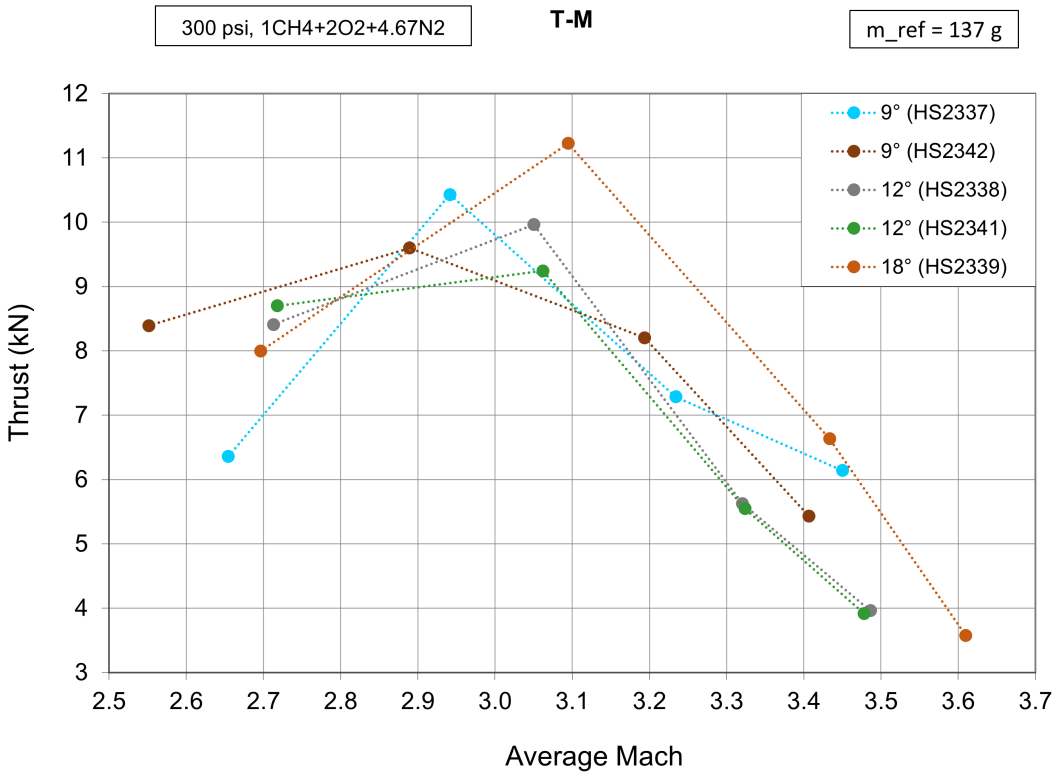

Figure 4.2: Nosecone thrust-mach data

Shots HS2338 (in gray) and HS2341 (in green) both represent the P380-2BL-12-12 projectile and show very good agreement in thrust vs. Mach number behavior with a maximum deviation from average thrust of $\approx 8\%$ at Mach = 3.05. This gives us confidence in the repeatability of our test method and projectile geometries. The P380-2BL-12-09 projectile was also repeated in shots HS2337 (blue) and HS2342 (dark brown) and showed more scat-

ter in their data. This could be influenced by the $\approx 7\%$ difference in start velocity (HS2342 entered at a lower velocity due to poor diaphragm opening).

Table 4.1 shows a summary of pertinent performance data from the six nosecone test cases. All velocities were calculated using the aforementioned distance-time method and then used to derive values for average thrust and acceleration over the 8-m-long test section. Masses were measured to the nearest hundredth of a gram but are shown rounded here. Note, on an 8-m basis, the average thrust of the 9° and 12° nosecone tests varied by less than 3% and 0.3% respectively, which indicates the thrust measurements were accurate enough to resolve the effects of these geometry variations.

Table 4.1: Nosecone series data, 8-m-long BTRA stage, $CH_4 + 2O_2 + 4.67N_2$ at 300 psi.

Shot #	Nose (°)	V_{in} $(\frac{m}{s})$	V_{out} $(\frac{m}{s})$	ΔV $(\frac{m}{s})$	Thrust (N)	Accel (g)	Mass (g)
HS2334	15	922	1282	360	6833	5095	137
HS2337	9	895	1250	355	7499	4886	156
HS2338	12	898	1253	355	6904	4899	144
HS2339	18	890	1295	406	7378	5686	132
HS2341	12	898	1250	352	6860	4848	144
HS2342	9	842	1231	389	7919	5175	156

Figure 4.3 shows a comparison of pressure traces from the 9° (4.3a) and 18° (4.3b) nosecone projectiles. These two projectiles represent the most extreme ends of the nosecone geometry variation and therefore will show the greatest differences in their pressure fields. The probe used for this comparison was located at station 13, 3-m from the entrance to the BTRA test section, and was chosen both for its location (roughly halfway through the system) and for the quality of its signals. The x-axis shows signal time (in milliseconds) and the y-axis shows signal strength (in volts). Pressures are obtained using a conversion factor of 12,500 psi/V.

Highlighted in the figures are the location and magnitude of the oblique shock from

the nose of the projectile (first drop) and the location and magnitude of the combustion waves at the base of the projectile (large peaks). The vertical line in red denotes the time when the adjacent mag probe detected the projectile passage. These data are useful in understanding the state of the flowfield surrounding the projectile as well as the location and relative strengths of shocks. The two traces showed a noticeable difference in the shape and magnitudes of their oblique shocks with the 9° and 18° nosecones having 960 psi and 1,925 psi, respectively. The trailing combustion waves were similar in shape and magnitude with those from the 9° nose peaking at 5,200 psi and those from the 18° nose peaking at 7,300 psi.

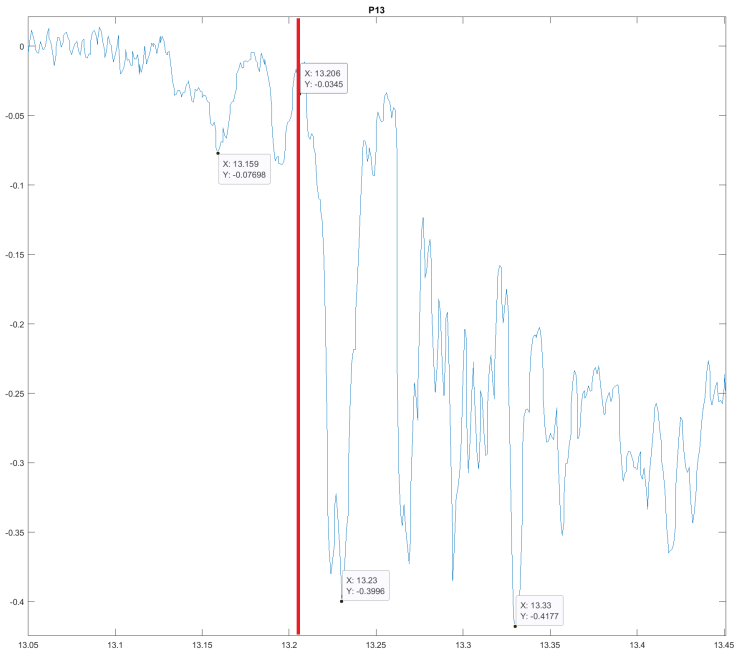

(a) HS2337, 9° nosecone

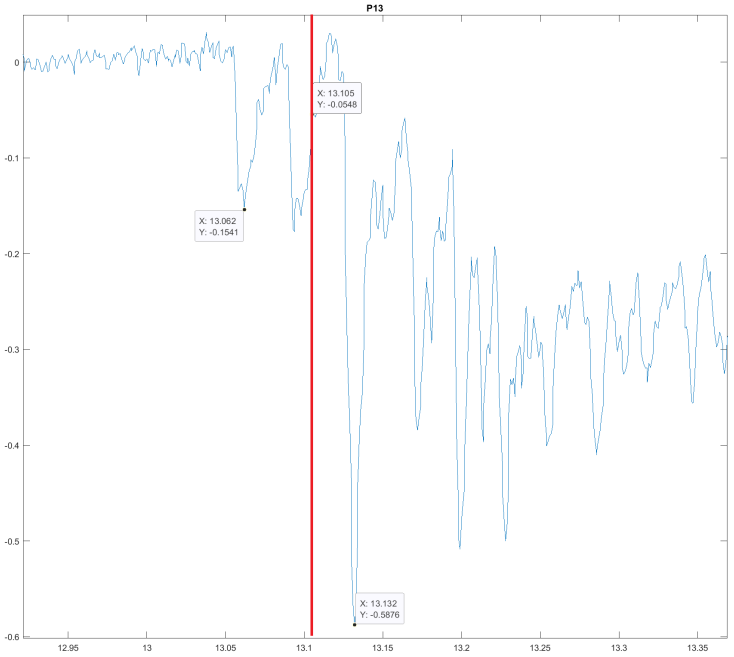

(b) HS2339, 18° nosecone

Figure 4.3: Comparison of nosecone series pressure traces

4.1.2 Tailcone Series

The tailcone series consisted of data from five individual shots, one for each of the four variations and one repeat shot. The entrance velocities ranged from 807 to 901 m/s. Of these, three of the shots had entrance velocities in range 898-901 m/s with the outlier being HS2347 (shown in pink) that entered roughly 100 m/s below target due to poor diaphragm opening. The peak velocity at the BTRA exit of this test series was $V_{out} = 1313$ m/s which was observed on the 9° tailcone (P380-2BL-09-15). This projectile had a total delta-v of 413 m/s, second only to the 18° tailcone projectile (P380-2BL-18-15) which managed 415 m/s. Note that the 12° tailcone reference projectile was excluded from these plots due to variance in its performance that implied severe projectile degradation had occurred.

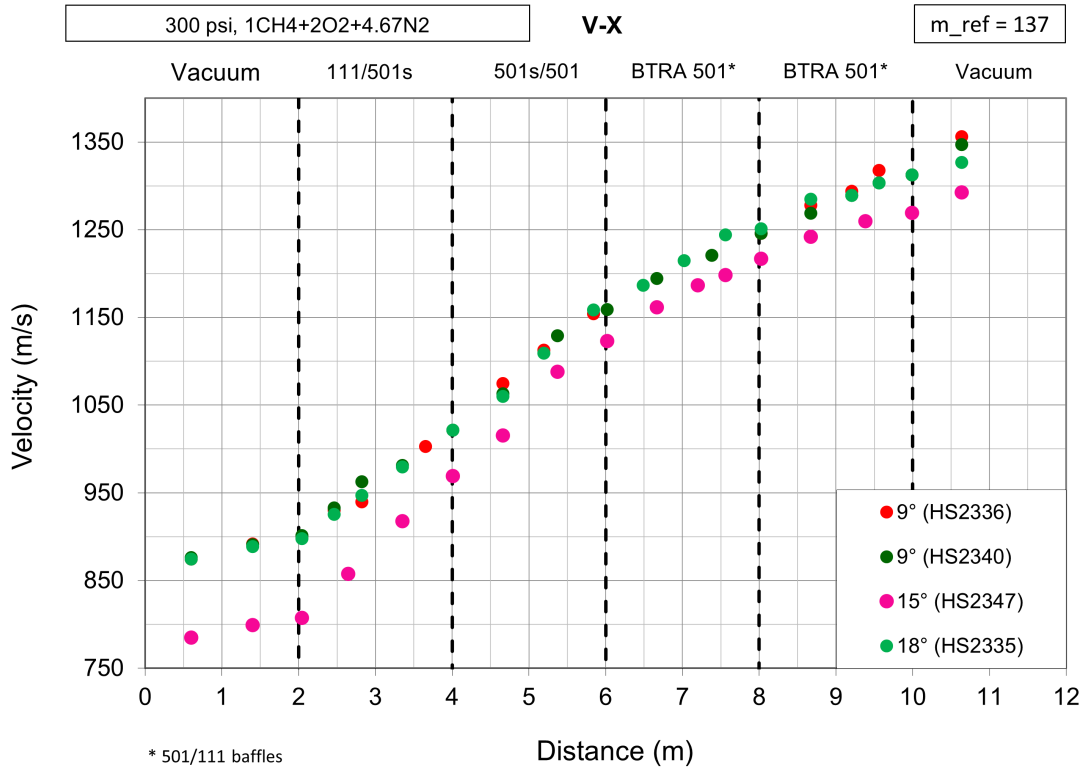

Figure 4.4: Tailcone velocity-distance data

Overall, the velocity-distance data were very similar for all projectiles, with differences

only visible in the final portion of the test section (tube 4) where the two 9° tailcone projectiles maintained higher thrust levels than their short-tailed counterparts. These differences can be seen more clearly in the thrust-Mach plot shown in Figure 4.5 where the projectiles with 9° tailcones (shown in dark green and red) have a higher peak thrust and more gradual thrust dropoff. While the sustained performance of the 9° tailcone projectile was repeated in its second shot the 18° tailcone projectile (shown in light green) also outperformed baseline in the final stage. Thus it was not clear whether tailcones that were longer or shorter than the baseline were better for BTRA applications.

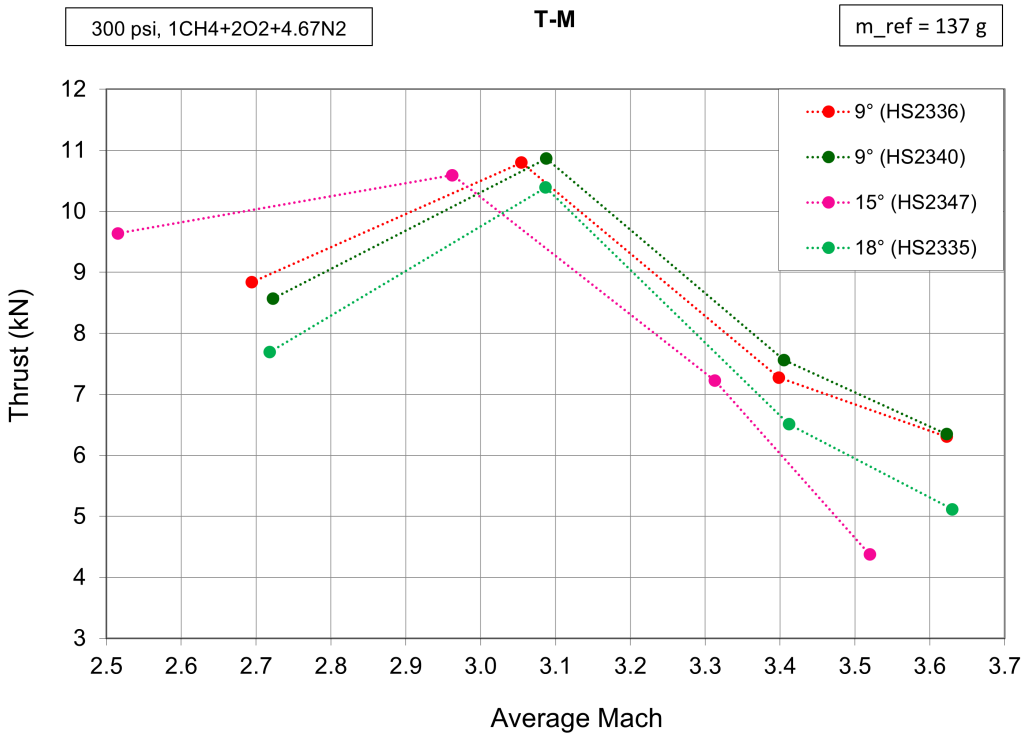

Figure 4.5: Tailcone thrust-Mach data

The differences in performance are greatest in the initial stage (where starting effects impact) and in the final stage (where projectile degradation becomes a factor). This indicates that projectiles are less sensitive to a change in tailcone angle than nosecone angle, which was expected. The 8-m average thrust and acceleration are listed in Table 4.2. Note that

the two 9° tailcone projectiles had entrance velocities within 1 m/s of each other, identical exit velocities, and an 8-m average thrust difference of only 0.3%. This gives us confidence that the thrust measurements were accurate enough to resolve the effects of these geometry variations.

Table 4.2: Tailcone series data, 8-m-long BTRA stage, $CH_4 + 2O_2 + 4.67N_2$ at 300 psi.

Shot #	Tail (°)	V_{in} $(\frac{m}{s})$	V_{out} $(\frac{m}{s})$	ΔV $(\frac{m}{s})$	Thrust (N)	Accel (g)	Mass (g)
HS2334	12	922	1282	360	6833	5095	137
HS2335	18	898	1313	415	7351	5878	127
HS2336	9	900	1313	413	8321	5859	145
HS2340	9	901	1313	411	8347	5840	146
HS2347	15	807	1269	462	7969	6147	132

Figure 4.6 shows a comparison of pressure traces from the 18° (4.6a) and 9° (4.6b) tailcone projectiles. These two are shown as they represent the most extreme ends of the tailcone geometry variation and therefore will show the greatest differences in the trailing edge pressure field. As with the nosecone series, these traces were taken from a pressure transducer at station 13. The plots show time on the x-axis (in milliseconds) and signal strength on the y-axis (in volts), and can be converted to pressure using a conversion factor of 12,500 psi/V.

Highlighted in the figures are the location and magnitude of the oblique shock from the nose of the projectile (first drop) and the location and magnitude of the combustion waves at the base of the projectile (large negative voltage peaks). The vertical line in red denotes the time when the adjacent mag probe detected the projectiles passage. The two traces showed lead oblique shocks of similar shape and magnitude with the 18° tail having an oblique shock peak of 1,800 psi and the 9° tail having an oblique shock peak 2,000 psi. The trailing combustion waves showed a noticeable difference in shape and magnitude with the 18° tail peaking at 12,800 psi and the 9° tail peaking at 6,800 psi.

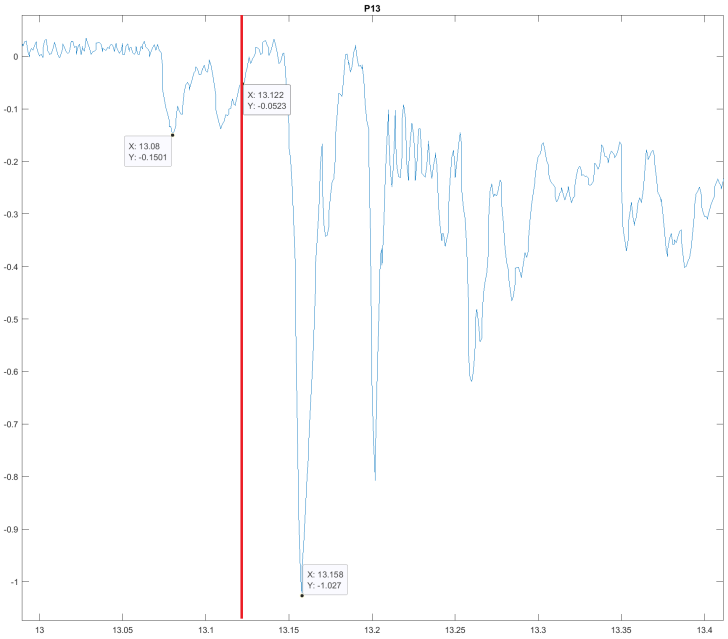

(a) HS2335, 18° tailcone

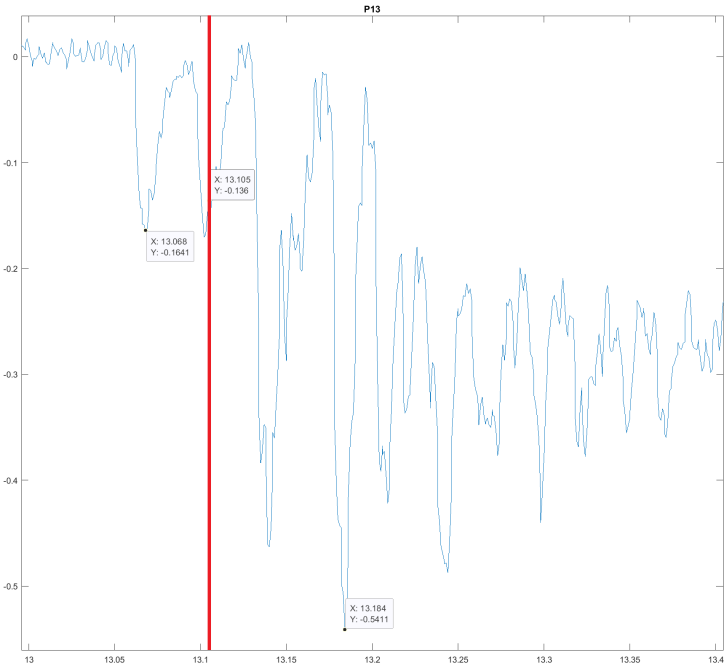

(b) HS2336, 9° tailcone

Figure 4.6: Comparison of tailcone series pressure traces

4.1.3 Diameter Series

The diameter series consisted of data from five individual shots, one for each of the diameter variations. Entrance velocities ranged from 813 to 860 m/s. The peak velocity was V_{out} = 1330 m/s which was observed on both the 1.40-in diameter (P400-2.5BL-12-15) as well as the 1.34-in diameter (P340-3BL-12-15). However, of these, the 1.40-in projectile had a greater total delta-v of 517 m/s, compared with the 1.34-in projectile which had 470 m/s. Velocity-distance data can be seen in Figure 4.7. Note that the data from these experiments includes variations in both diameter and projectile shoulder length as shown in Table 4.3.

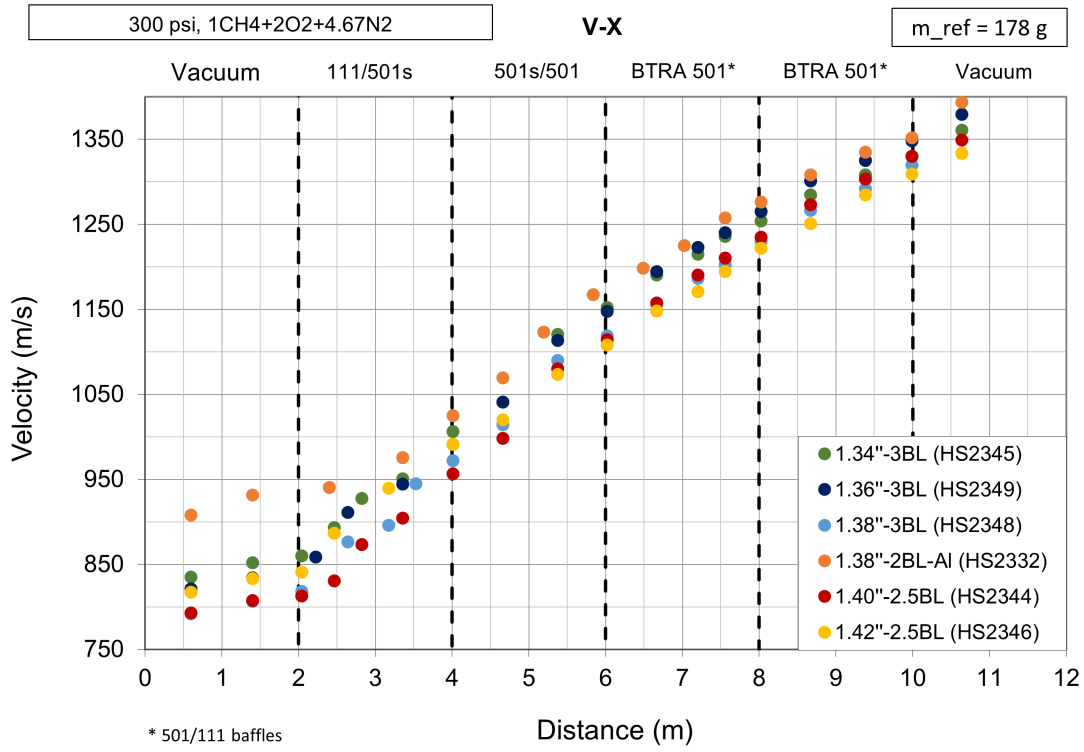

Figure 4.7: Diameter velocity-distance data

A plot of thrust vs. Mach can be seen in Figure 4.8. From this plot we can see a clear difference in the thrust profile as a function of shoulder length and diameter. Peak thrust was 14.1 kN and was recorded in stage 2 with the 1.36-3BL projectile (shown in dark blue).

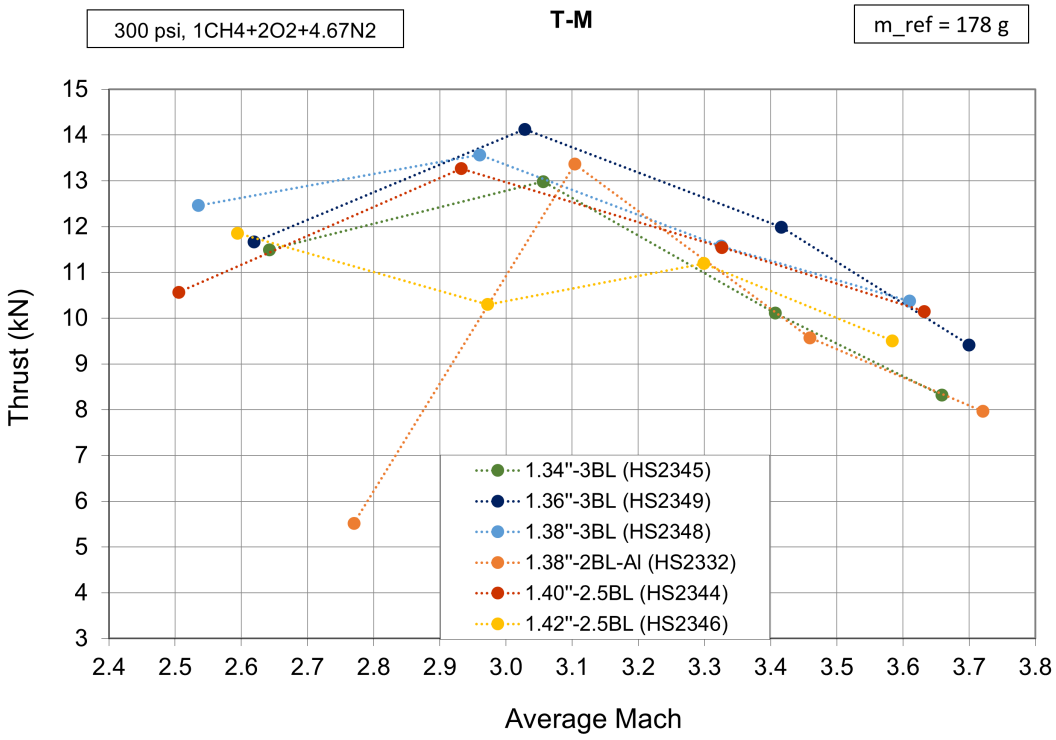

Figure 4.8: Diameter thrust-Mach data

Table 4.3: Diameter series data, 8-m-long BTRA stage, $CH_4 + 2O_2 + 4.67N_2$ at 300 psi.

Shot #	Dia (in)	V_{in} $(\frac{m}{s})$	V_{out} $(\frac{m}{s})$	ΔV $(\frac{m}{s})$	Thrust (N)	Accel (g)	Mass (g)
HS2344	1.40-2.5BL	813	1330	517	11391	7110	163
HS2345	1.34-3BL	860	1330	470	10737	6603	166
HS2346	1.42-2.5BL	841	1309	468	10713	6457	169
HS2348	1.38-3BL	818	1320	501	12001	6873	178
HS2349	1.36-3BL	859	1348	490	9190	5512	170

Figure 4.9 shows a comparison of pressure traces from the 1.34-in (4.9a) and 1.42-in (4.9b) diameter projectiles. These two are shown as they represent the most extreme ends of the diameter geometry variation and therefore will show the greatest differences in the trailing edge pressure field. As with the nosecone and tailcone series, these traces were taken from a pressure transducer at station 13. The plots show time on the x-axis (in milliseconds) and signal strength on the y-axis (in volts), and can be converted to pressure using a conversion factor of 12,500 psi/V. Highlighted in the figures are the location and magnitude of the oblique shock from the nose of the projectile (first drop) and the location and magnitude of the combustion waves at the base of the projectile (large peaks). The vertical line in red denotes the time when the adjacent mag probe detected the projectiles passage. The two traces showed oblique shocks of roughly similar magnitude with the 1.34-in diameter having an oblique shock peak of 1,500 psi and the 1.42-in diameter having an oblique shock peak 1,900 psi. However, the two pressure traces showed a distinct difference in shape, with the 1.34-in showing clear shock impingements while the 1.42-in did not. The trailing combustion waves showed a noticeable difference in shape and magnitude with the 1.34-in diameter peaking at 5,800 psi and the 1.42-in diameter peaking at 11,800 psi.

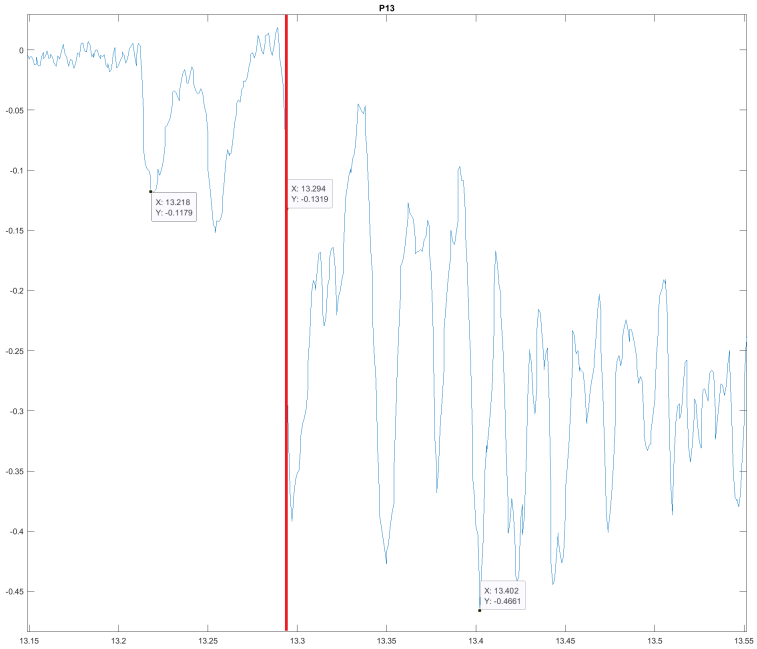

(a) HS2345, 1.34-3BL

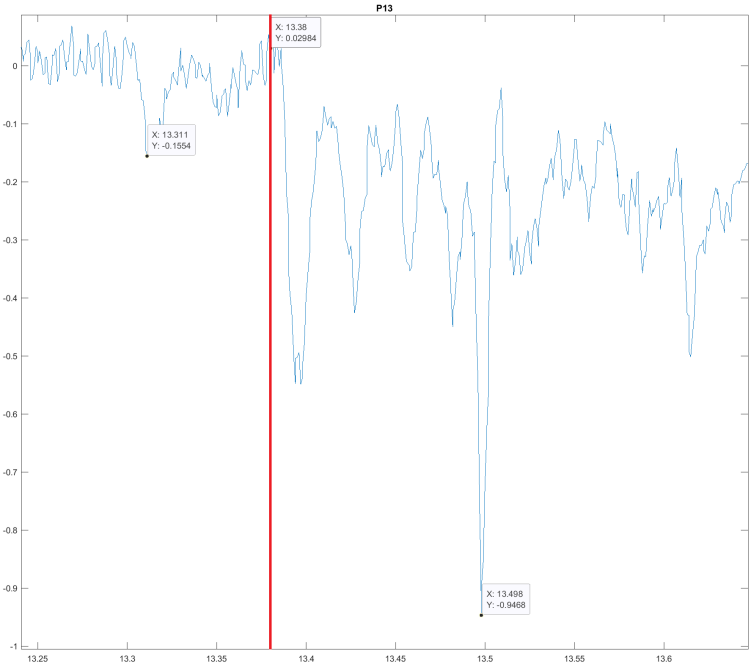

(b) HS2346, 1.42-2.5BL

Figure 4.9: Comparison of diameter series pressure traces

4.2 Analysis

The data from each of the three geometry variation series are analyzed and compared with prior results in this section.

4.2.1 Nosecone Series Analysis

In order to better understand the nosecone angle thrust trends, 8-m averaged thrust was plot against nosecone angle as shown in Figure 4.10. This appears to show that both large angle (short) and small angle (long) nosecones offer performance benefits.

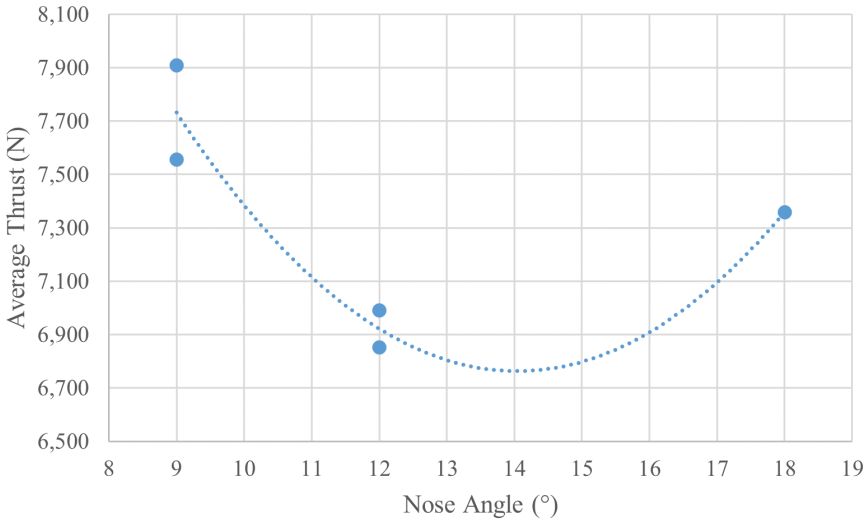

Figure 4.10: Nosecone 8-m average thrust comparison

In an effort to explain the relationships seen in Figure 4.10, relative thrust was plot on a per-tube basis as shown in Figure 4.11. Relative thrust was calculated by relating to a reference shot, HS2332, which was a P380-2BL-12-15 manufactured out of aluminum. This shot was chosen as a reference since it was known to be in good agreement with prior experiments and less susceptible to projectile degradation than Lexan projectiles. In this plot, T1, T2, T3, and T4 denote the relative thrusts in baffle tubes 1-4 respectively, while "Ref" denotes the reference projectile's thrust. From this plot we see can see an interesting

evolution of performance. In the first ram stage, thrust data is scattered and inconsistent, likely due to the influence of starting effects. Once past tube 1, we see that thrust is initially higher at higher nosecone angles prior to dropping off in tube 3 and 4 where less steep nosecone angles are seen to perform better.

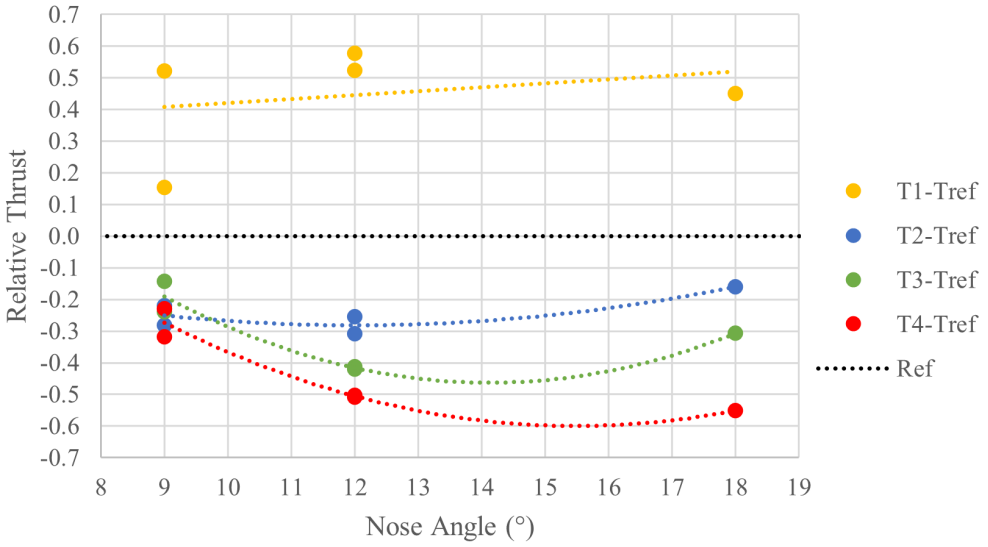

Figure 4.11: Nosecone relative thrust comparison

This behavior could be explained by the longer nosed projectiles having a start delay (leading to low initial thrust) but then outperforming their shorter counterparts at high Mach numbers due to lower wave drag. Longer nosed projectiles (smaller nosecone angle) should have less wave drag than their shorter (large angle) counterparts. This is because they will have a shallower oblique shock angle and therefore less pressure rise across the shock. This relationship is described by the oblique shock equations for wave angle, β, and pressure ratio as shown below:

$$\frac{\tan(\beta-\theta)}{\tan(\beta)} = \frac{2+(\gamma+1)M_1^2\sin^2(\beta)}{(\gamma+1)M_1^2\sin^2(\beta)} \tag{4.1}$$

$$\frac{p_2}{p_1} = \frac{2\gamma M_1^2\sin^2(\beta)-(\gamma-1)}{\gamma+1} \tag{4.2}$$

From these equations we see that by increasing the nosecone angle, θ, we will also increase the shock angle, β and therefore the pressure ratio which determines wave drag and possibly impacts starting dynamics. Note that, as shown in our pressure comparison Figure 4.3, the shortest nosecone projectile (18°) had a recorded oblique shock magnitude of 1925 psi which was more than double that of the longest nosecone projectile (9°) at 960 psi. It was also found that the combustion pressure waves showed similar structures and magnitudes which implies that nosecone angle does not have a major effect on the combustion region once the ram cycle has started.

4.2.2 Tailcone Series Analysis

In order to better understand the tailcone angle thrust trends, 8-m averaged thrust was plot against tailcone angle as shown in Figure 4.12. From the plot, we see that thrust decreases with tailcone length.

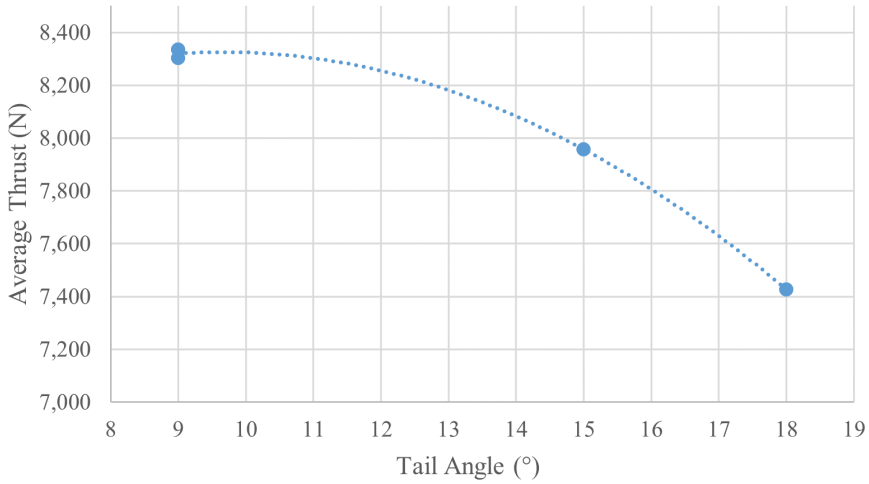

Figure 4.12: Tailcone 8-m average thrust comparison

As with the nosecone series, relative thrust was plot on a per-tube basis as shown in Figure 4.13 by relating to the same P380-2BL-12-15 aluminum reference shot, HS2332. Here T1, T2, T3, and T4 denote the relative thrusts in baffle tubes 1-4 respectively, while "Ref"

denotes the reference projectile's thrust. From this plot we see can see an interesting trend in performance. As with the nosecone series, thrust data in the first ram stage is more scattered and inconsistent, likely due to the influence of starting effects. Once past tube 1, we see that thrust decreases slightly with increasing nosecone angle in all three tubes.

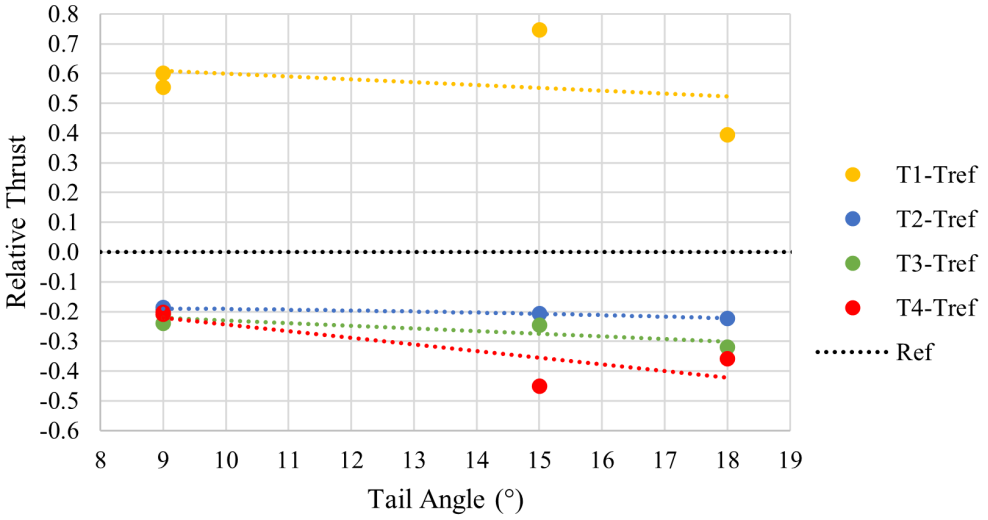

Figure 4.13: Tailcone relative thrust comparison

Note that, as shown in our pressure comparison Figure 4.6, the shortest tailcone projectile (18°) had a recorded combustion wave peak magnitude of 12,800 psi which was nearly double that of the longest tailcone projectile (9°) at 6,800 psi. However, both tailcone variations showed oblique shock traces with similar structures and magnitudes which implies that tailcone angle effects the trailing combustion wave but does not have a major influence on the flowfield in front of the projectile. Because the longer tail had higher average thrust with lower driving pressures, it is possible that its projectile drag may be less. It is not clear if we can assume the thrust is proportional to the peak pressure measured at the tube wall behind the projectile. Nonetheless, on-going CFD efforts are investigating this issue.

4.2.3 Diameter Series Analysis

As with the nosecone series, 8-m averaged thrust was plot against shoulder diameter as shown in Figure 4.14. This plot also has variations in projectile shoulder length and material, with a 2BL aluminum projectile shown in orange, 2.5BL Lexan in gray, and 3BL Lexan in blue.

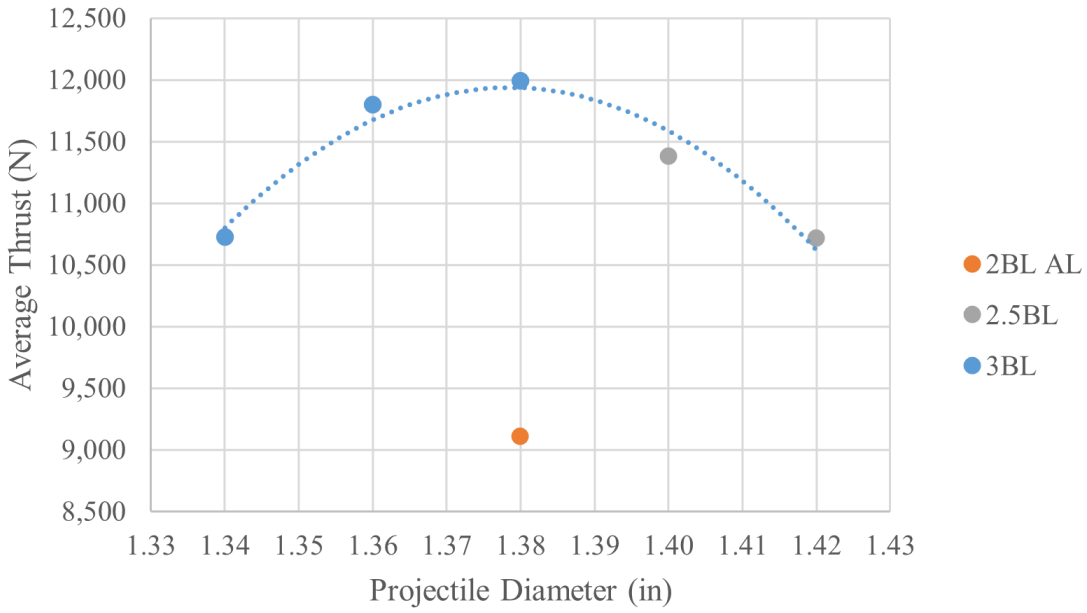

Figure 4.14: Diameter 8-m average thrust comparison

From the plot, we see clear trend that 1.38-in is the optimal diameter for our configuration and that longer shoulder lengths allow for higher average thrust. We compare this with two prior studies; one on projectile diameter Figure 4.15, and one on projectile shoulder length, Figure 4.16.

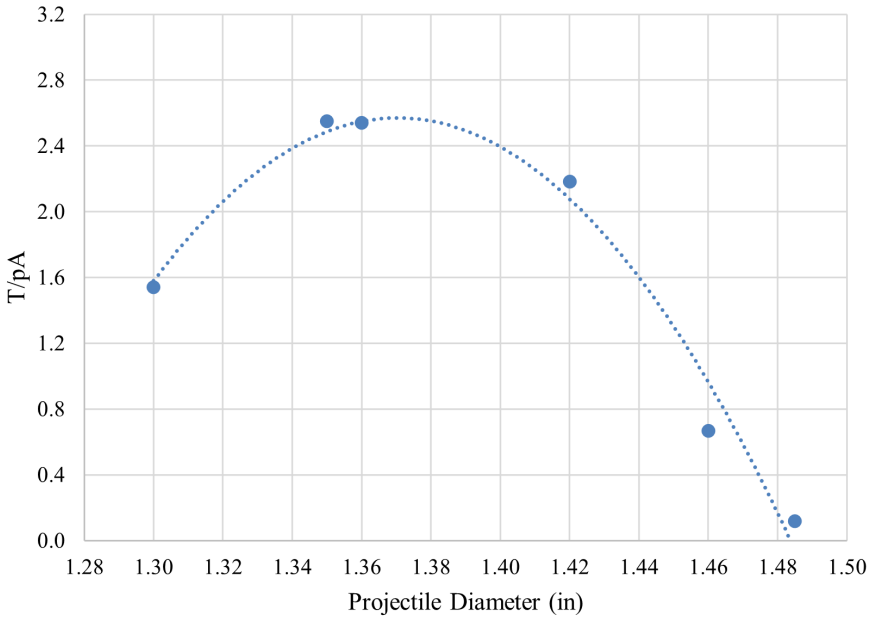

Figure 4.15: Inward slanted baffles normalized thrust comparison for 2-m-long stage at BTRA entrance

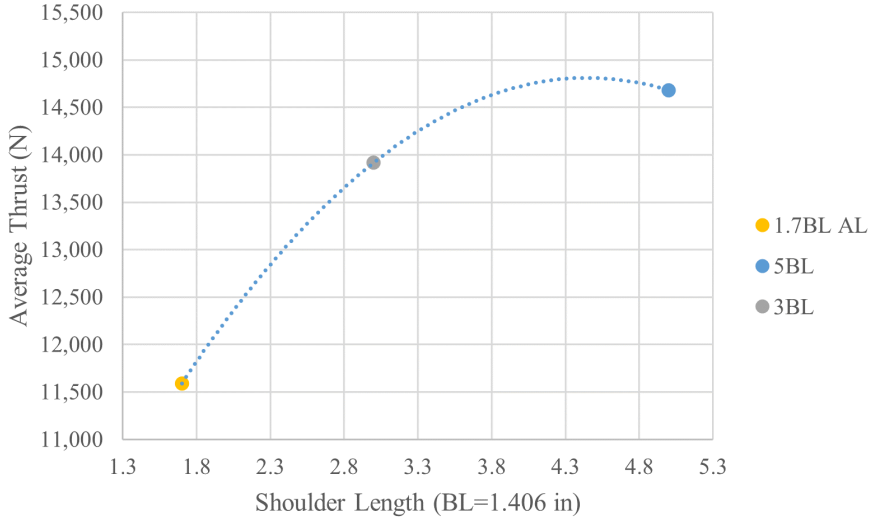

Figure 4.16: Shoulder length 8-m average thrust comparison

The prior diameter series tested projectiles with diameters in the range 1.30-1.485. While this series never tested a 1.38-in projectile, it identified a trend indicating this was the optimal geometry. The experiments in this study differed in that they used slanted baffles, a fuel-rich mixture, 1.5BL projectiles, and a BTRA test section length of only 2-m [10]. The plot shown is normalized with respect to pressure and bore area and has the same trend as Figure 4.14.

The prior shoulder length series tested projectiles with shoulder lengths ranging from 1.7BL to 5BL. This series had the same chemistry and fill pressure as the current study, but used a different baffle configuration [9]. As shown in the figure above, thrust was found to increase with increasing shoulder length over all lengths tested.

As shown in our pressure comparison, Figure 4.9, the smallest diameter projectile (1.34-in) had a recorded combustion wave peak magnitude of 5,800 psi which was less than half that of the largest diameter projectile (1.42-in) at 11,800 psi. Both diameter variations showed oblique shock traces with similar magnitudes but differing structures. This matches our expectation that larger diameter projectiles (which have a smaller throat) can better contain large pressures at the base of the projectile.

Chapter 5
CONCLUSIONS

5.1 Conclusion

The influence of projectile geometry on baffled tube ram accelerator performance was investigated in an effort to identify the optimum projectile geometry. Geometric variations included the nosecone angle, tailcone angle, projectile shoulder diameter, and projectile shoulder length. This investigation found that longer nosecones perform better at high Mach numbers, likely due to decreased wave drag. Shorter nosecones were found to perform better at low Mach numbers, possibly due to higher pressures enabling a faster ram start. Thrust was found to increase with increasing tailcone length and noticeable differences in combustion flowfield were recorded suggesting that this should be investigated further. The 1.38-3BL projectile was confirmed to be the best performing, however, its worth noting that the 1.40-2.5BL had close performance suggesting that there is a small range of shoulder diameters with nearly the same thrust performance. Thrust was found to increase with increasing shoulder length, and at this point there does not appear to be any limit to shoulder length for robust BTRA operation.

5.2 Future Work

Additional analysis of pressure and time data could establish a more complete understanding of the flowfield history. This could be combined with analytical calculations to yield verification of the wave drag theory and its implications for nosecone angle. Further tailcone geometries could be explored by varying the base diameter of the projectile. Lastly, since no definite limit on projectile shoulder length has been found, testing of projectiles with greater shoulder lengths would add valuable data.

BIBLIOGRAPHY

[1] C. Knowlen, J. F. Glusman, R. Grist, A. P. Bruckner, and A. J. Higgins. Experimental investigation of a baffled-tube ram accelerator. *52nd AIAA/SAE/ASEE Joint Propulsion Conference*, Salt Lake City, UT, July 25-27, 2016. doi:10.2514/6.2016-4813.

[2] A. Hertzberg, A. P. Bruckner, and D. W. Bogdanoff. Ram accelerator: A new chemical method for accelerating projectiles to ultrahigh velocities. *AIAA Journal*, 26(2):195–203, February 1988.

[3] Carl Knowlen. Direct space launch using ram accelerator technology. In *AIP Conference Proceedings*. AIP, 2001. doi:10.1063/1.1357980.

[4] Mark Russell, Rob Urselmann, Desiree Bernhard, Brooke Colburn, Charles Russell, and Kaito Durkee. Robotic mining and micro tunneling using hypersonic projectile impact technology field trial results, technical evaluation and economic valuation. In *RETCON Conference Proceedings*, 06 2021.

[5] Abraham Hertzberg, Adam P. Bruckner, and C. Knowlen. Experimental investigation of ram accelerator propulsion modes. *Shock Waves*, 1:17–25, 1991.

[6] A. J. Higgins, C. Knowlen, and A. P. Bruckner. Ram accelerator operating limits, part 1: Identification of limits. *Journal of Propulsion and Power*, 14(6):951–958, November 1998.

[7] A. J. Higgins, C. Knowlen, and C. B. Kiyanda. Gasdynamic operation of baffled tube ram accelerator in highly energetic mixtures. *20th International Colloquium on the Dynamics of Explosions and Reactive Systems*, Montreal, Canada, 2005.

[8] Thomas Imrich. The impact of projectile geometry on ram accelerator performance. MSAA, University of Washington, 1995.

[9] John P. Correy, Brian J. Leege, Desiree Bernhard, Jason Ginos, Cullen Yancey, Carl Knowlen, and Andrew J. Higgins. Investigation of baffled-tube ram accelerator configurations. In *AIAA SCITECH 2023 Forum*. American Institute of Aeronautics and Astronautics, jan 2023. doi:10.2514/6.2023-2186.

[10] Trever Byrd. Experimentally-driven model for the baffled-tube ram accelerator. MSAA, University of Washington, 2018.

[11] A. P. Bruckner, C. Knowlen, A. Hertzberg, and D. W. Bogdanoff. Operational characteristics of the thermally choked ram accelerator. *Journal of Propulsion and Power*, 7(5):828–836, September 1991. URL: `https://doi.org/10.2514/3.23398`.

[12] Vincent Tanguay and Andrew Higgins. On the inclusion of frictional work in non-ideal detonations. *19th International Colloquium on the Dynamics of Explosions and Reactive Systems*, Montreal, Canada, 2005.

[13] A. Hertzberg, A. P. Bruckner, and C. Knowlen. Experimental investigation of ram accelerator propulsion modes. *Shock Waves*, 1(1):17–25, March 1991. `doi:10.1007/bf01414864`.

[14] A. Sasoh, Y. Hamate, and K. Takayama. Small-bore ram accelerator operation. *Journal of Propulsion and Power*, 17(3):622–628, May 2001. `doi:10.2514/2.5788`.

[15] C. Knowlen, P. Bauer, T. Bengherbia, Y. Yao, A.P. Bruckner, and M. Giraud. Unsteady 1-d thrust modeling with eos effects for ram accelerator experiments at different bores. *The J. of Aerospace Science, Technology and Systems*, 97(1):19–26, 2018.

[16] Cullen Yancey. Performance modeling of the baffled tube ram accelerator. MSAA, University of Washington, 2022.